Article

# Atomistic Simulation of Primary Radiation Damage Profiles in Fluorine-Doped Tin Oxide Thin Film Target Using SRIM Code

**Bosco Oryema**[1]
https://orcid.org/0000-0002-6054-1269
b.oryema@muni.ac.ug

**Itani G. Madiba**[2,3]
https://orcid.org/0000-0002-7091-9202

**Christopher B. Mtshali**[2]
https://orcid.org/0000-0001-5044-5575

## Abstract

In this study, we investigated the discrepancy between the numbers of atomic displacements obtained from the Vac.txt method and those obtained from the Vac.dam method using SRIM-2013 operated in full cascade mode. The SRIM simulations also calculated energy partitioning, damage dose and distribution profiles of the implanted He, C and O ions at three different ion energies of 10 keV, 100 keV and 1 MeV. In all the simulations and at each ion energy value, the target thickness was increased until the entire ion beam was absorbed within the target. The simulated fluorine-doped tin oxide (FTO) thin film target stoichiometrically comprised 78.6% Sn, 16.4% O and 5.0% F, and a 6.013 g/cm$^3$ bulk density. To achieve relatively good statistics with compromised computational time, each run followed 10 000 ion histories. The results indicated that, with increasing ion energies, the peaks of vacancy concentrations moved deeper into the material. For He ions, the vacancy profiles have peaks at ~0.04, ~0.45 and ~2.9 μm at 10 keV, 100 keV and 1 MeV, respectively. Meanwhile, for C and O ions, the peaks were at ~0.012, ~0.15 and ~1.23 μm for C ions and ~0.01, 0.12 and 1.2 μm for O ions at 10 keV, 100 keV and 1 MeV, respectively. We also observed that for all the ions and at all ion energies considered, the Vac.txt method predicted more vacancies than the Vac.dam method, and the discrepancies generally increased with increasing Z by an average value of ~1.21, ~1.45 and 1.48 for He, C and O ions respectively.

1 Department of Physics, Muni University, Uganda.
2 Tandetron Laboratory, iThemba LABS–National Research Foundation, South Africa.
3 UNESCO–UNISA Africa Chair in Nanoscience and Nanotechnology, College of Graduate Studies, University of South Africa.

UNISA university of south africa PRESS
*Nano-Horizons*
Volume 3 | 2024 | 23 pages

Nano-Horizons
https://doi.org/10.25159/3005-2602/15610
ISSN 3005-2602 (Online)
© The Author(s) 2024

Published by Unisa Press. This is an Open Access article distributed under the terms of the Creative Commons Attribution 4.0 International License (https://creativecommons.org/licenses/by/4.0/)

In addition, the electronic and nuclear partitioning profiles revealed that most of the energies of the ions were lost in collision with atomic electrons due to ionisation and excitations, and little to nuclear events. The simulations also revealed that nuclear stopping powers increase at low ion energies. This study also indicated that damage dose profiles strongly depend on the type of incident particle and its energy. A comparison of SRIM and iradina calculated vacancies and incident ion distribution profiles generally indicated perfect agreements between the two codes. FTO thin film remains a promising material for thermal control applications in future spacecraft. However, further analyses are still necessary to comprehensively understand its evolution under intense radiation environments comprising various ions and at different energies.

**Keywords:** Fluorine-doped tin oxide, SRIM code, iradina code, displacement per atom, energy partitioning, binary collision approximation.

## 1 Introduction

Fluorine-doped tin oxide (FTO) thin film has been proposed for passive thermal control coating (TCC) application in future miniaturised spacecraft. This is majorly owed to its high reflectivity in the infrared (IR) region, high stability in atmospheric conditions, high mechanical strength, chemical inertness, and high-temperature durability [1], [2], [3]. Some other well-known applications of FTO for the development of technological devices are its use as flat panel displays [4], touch screens [5], transparent light-emitting diodes [3], gas sensors, smart windows [6], solar cell electrodes [7] and transistors [8]. Although FTO may possess the desired qualities for TCC application, it is important to note that the space environment is not as free as imagined. This is because spacecraft operating in this environment are continuously bombarded by different types, energies and doses of ionising radiations originating from the galactic sources, the sun and secondary/tertiary radiations produced by the interactions of galactic and solar particle radiations with space objects [9], [10], [11]. Space radiations can cause dreadful defects such as dislocation loops, segregates, faults, precipitates, bubbles and voids in the microstructures of spacecraft components and subsystems [7], [12], [13], [14].

Proper quantification and understanding of radiation-induced defects in FTO thin film is therefore vital for determining its suitability for application in the space environment as a spacecraft passive TCC. Currently, powerful in situ and ex situ characterisation methods exist to observe and provide information about defect densities, sizes and types in materials under irradiation. They include but are not limited to transmission electron microscopy (TEM), optical microscopy, atomic force microscopy (AFM), Raman spectroscopy, X-ray photoelectron spectroscopy, scanning electron microscopy (SEM), small-angle neutron scattering (SANS), deep-level transient spectroscopy (DLTS) and positron annihilation spectroscopy (PAS) [15], [16].

However, tracking and characterising the formation and evolution of primary defects in materials under irradiation are so complex that the above techniques may not have the

required resolutions to image individual defects as they happen, and may not capture the temporal development of cascades. This is because the underlying atomistic mechanisms take place within a short lifetime in the order of picoseconds and a small volume dimension scale in the order of $nm^3$ [16], [17], [18], [19]. For instance, TEM is sometimes disadvantaged by the electron-beam radiation damage in materials and the small area for observation [15]. DLTS experiments can only characterise point defects at deep levels [16]. Also, when operated ex situ, these instruments can only rely on postmortem analyses of detectable defects to bring partial insights into what could have occurred during displacement cascades [17]. In addition, an ex situ study can only capture a limited number of snapshots of the materials during a physical process, while some key information between the interval of two snapshots may be missing [15]. Lastly, the instruments may be too expensive to acquire, operate and maintain.

The aforementioned limitations in experimental techniques have led to the birth and increased use of theoretical computational approaches by the ion-beam community for radiation damage simulations. Besides providing the physical basis for understanding and analysing the atomic-scale processes occurring during primary damage production and evolution events, computer simulations also allow one to study a large volume of the many-dimensional parameters for ion interactions, while providing sufficient information, such as implantation depth and damage profiles [16], [17], [19]. The most commonly used codes by the ion beam community to simulate radiation damage profiles in materials are the binary collision approximation (BCA) codes [15], [17], [20]. Other existing computational techniques not discussed in this study are molecular dynamics (MD), rate theory or rate equations, Monte Carlo neutronics (MCN), Metropolis Monte Carlo (MMC), discrete dislocation dynamics (DDD), kinetic Monte Carlo (KMC) and density function theory (DFT) methods [16], [19], [20].

The BCA method provides detailed information about the statistical defect distribution by assuming only two-body elastic interactions (binary collisions) between the incoming energetic ion and the closest target atom in its neighbourhood [21], [22]. BCA calculations are statistically accurate for a wide range of materials and ion energies and can treat large systems of particles [17], [18], [21]. Currently, several BCA-based computer programs are in existence. The Stopping and Range of Ions in Matter (SRIM) code, which includes the Transport of Ions in Matter (TRIM) subroutine, is the most widely used BCA software to compute ion trajectories and damages of different ion types with eV to GeV energies for various kinds of materials [16], [21], [23]. The other modern existing BCA codes include but are not limited to MARLOWE [22], iradina [24], [25], TRIM.SP [26], IM3D [15], [25], TRIDYN, TRI3DYN [27], MyTRIM, and SDTrimSP [21]. According to Agarwal et al. [23], the SRIM code has been used so often by the ion beam community for many years that it has become an unofficial standard and reference for the BCA estimation of damage. The primary reasons are that the software is free and comes with an amicable graphical user interface, which makes it easy to use [28]. It also has an extensive high-quality stopping power database [23].

For these reasons, we used SRIM in the present study to estimate damage production and energy deposition profiles for different ions.

SRIM calculations are mostly performed via one of the two basic options, namely, the detailed calculation with full damage cascades (FC) mode and the ion distribution and quick calculation of damage (QC) mode [23], [29], [30], [31]. The FC option explicitly follows and accounts for not only the trajectories of incident ions but also the trajectories of each primary and secondary recoiling atom created by the incident ions until their energies become too low to initiate any displacement events [23], [32]. The QC option tracks and tallies the paths of incoming ions only. This option uses the Kinchin and Peace (KP) model [33] to calculate the number of secondary displacements according to the equation,

$$v_{KP}(E) = \begin{bmatrix} 0 & ; & E < E_d \\ 1 & ; & E_d \leq E < 2E_d \\ \frac{E}{2E_d} & ; & 2E_d \leq E < \infty \end{bmatrix} \quad (1)$$

where $E_d$ is the threshold displacement energy of the target material, and $E$ is the energy of the incident ion.

The KP model was later modified by Norgett, Robinson and Torrens [34], whose model was known as the NRT model, to cater for inelastic scattering (electronic) energy losses that occur between two elastic collision sites as proposed by Lindhard's theory of energy partitioning [21], [23], [29], [31]. Consequently, the modified KP model, also commonly known as the NRT model, uses damage energy (ie part of the incident ion energy $E$ that is dissipated in elastic collisions with lattice atoms) to calculate the number of atomic displacements or vacancies. In other words, the NRT model provides a method for converting a known value of damage energy into a corresponding number of atomic displacements according to the equation [28], [29], [30], [31],

$$v_{NRT}(T_{dam}) = \begin{bmatrix} 0 & , & T_{dam} < E_d \\ 1 & , & E_d < T_{dam} < 2E_d/0.8 \\ \frac{0.8T_{dam}}{2E_d} & , & 2E_d/0.8 < T_{dam} < \infty \end{bmatrix} \quad (2)$$

where $T_{dam}$ is the damage energy obtained from Lindhard's theory of energy partitioning, and the constant 0.8 is the correction factor of the hard-sphere approximation [35], [36], [37].

The NRT model has been widely regarded and accepted by the ion implantation community as the internationally recognised standard for quantifying the level of primary damage in irradiated materials. In this study, we therefore used SRIM software

operated in both FC modes to calculate the primary radiation damage defects in FTO films. The objectives of the current work were to calculate the depth-dependent vacancy distribution profiles, compare the SRIM FC Vac.txt and Vac.dam methods, and determine the energy partitioning, ion distribution and damage dose profiles of the implanted ions in the FTO films. We also compared the SRIM results with results obtained from the iradina code. It is important to note that this is the first research to report irradiation-induced damages in FTO thin films based on SRIM simulations. Defect production owing to He, C and O ions in materials intended for space applications is crucial because of their high fluxes in the deep space environment. Details of the simulation parameters used are provided in the next section.

# 2 Methodology

## 2.1 Simulation Parameters

Computer simulations of primary radiation damage defect production of He, C and O ions in FTO thin film were performed using the full-cascade (FC) option of SRIM software version 2013 [38]. These ions were selected because they form part of the most common and abundant species of ionising radiations found in the deep space environment [10], [11], [39]. The He, C and O ion beams were monoenergetic and unidirectional beams incident perpendicularly on the film's surface. The incident kinetic energies for all the ions varied from 10 keV to 1 MeV to investigate the energy dependence of vacancy and damage productions. These low energy values were chosen for convenience but are also typical for charged particle radiations found in the deep space environment [11], [40]. In all simulations and at each value of ion energy, the target thickness was increased until the entire ion beam was absorbed within the target. This means that the film thickness exceeded the maximum range of both the ions and recoils or any other secondary charged particles created.

The simulated FTO thin film target stoichiometrically comprised 78.6% Sn, 16.4% O, and 5.0% F [41], and a bulk density of 6.013 g/cm$^3$. Target elemental masses of 118.71 amu for Sn, 15.99 amu for O and 18.99 amu for F, and the incident ion masses of 4.003, 12.0 and 15.995 amu for He, C and O respectively were used for all calculations. To achieve relatively good statistics with compromised computational time, each run followed 10 000 ion histories [42]. To be consistent with the NRT defect production model as recommended by Stoller *et al*. [31], the lattice binding energies for all target elements (Sn, O and F) were set to zero. Surface binding energies of 3.61 eV for Sn, 6.79 eV for O and 2 eV for F [43] were used during all the calculations. The average threshold displacement energies of the target elements used in this study are 20 eV for Sn [44], 45 eV for O [44], [45], and 40 eV for F [44]. Based on these elemental threshold displacement energies, the effective displacement energy of the FTO target was calculated to be 22.6 eV using the empirical equation [23], [35],

$$E_{d,eff} = \left(\sum_i \frac{S_i}{E_{d,i}}\right)^{-1} \quad (3)$$

where $S_i$ and $E_{d,i}$ are the stoichiometric fraction and threshold displacement energy of the *i*th atomic species, respectively.

### 2.3 SRIM Vacancy and Damage Profile Calculations

Following the recommendation of Agarwal *et al*. [23], the vacancy and damage production profiles in this study were calculated using the SRIM FC damage energy approach, referred to as the "Vac.dam" method. They argue that this option generally provides the highest accuracy for vacancy production owing to the use of SRIM stopping powers for both the incident ions and all recoils and detailed tracking of all ion collisions within the BCA limitations. However, the well-known disadvantages associated with this method may include manual manipulation by the user of the SRIM data files that is necessary to calculate the damage energy, calculation of the effective damage energy needs to be performed for compounds, and vacancy production may be slightly underestimated for low PKA energy irradiation energy conditions [23]. In this study, for comparison, the number of vacancies obtained from the FC Vacancy.txt output file (as the sum of vacancies in all target elements), referred to as the "Vac.txt" method, was compared with those obtained from the FC "Vac.dam" method in all simulations.

The damage energy, $T_{dam}$, values used in this study were calculated from the "PHONON.txt" SRIM output file as the sum of ion and target recoil energies that go into phonons [25], [31], [35]. This damage energy method was favoured because it is more consistent with the definition of damage energy in the NRT model and is easy to calculate from the SRIM data files. The damage energy was then manually converted into displacement per atom (DPA) using the equation [21], [23],

$$DPA_{dam} = \left[\frac{0.8 \times T_{dam}}{2 \times E_{d,eff}}\right] \times \left[\frac{\emptyset \times 10^8}{N}\right] \quad (4)$$

where, $\emptyset$ and $N$ are particle fluence and target atomic density, respectively. $E_{d,eff}$ is the effective displacement energy, and the constant $10^8$ is the conversion factor from centimetre to angstrom [42].

In this study, we obtained the atom density of $3.73 \times 10^{22}$ atoms/cm$^3$ used from SRIM output. We used a constant ion fluence of $1 \times 10^{15}$ ions/cm$^2$ in the DPA calculations. We chose this fluence value for convenience to test the tolerance limit of FTO in extreme radiation environments since it is way above the average fluence of typical particles in the space environment, which is ~$10^{10}$ particles/cm$^2$ [46].

### 2.4 Validation of the SRIM Results

Although SRIM remains a preferred code among the ion beam community, it is known to have a few weaknesses. First, SRIM is not an open-source code; even the actual code is unknown to the users [21]. The details of its displacement and damage production algorithms are therefore not publicly accessible in its manual, which makes it difficult to reproduce SRIM results. For these reasons, it is worth validating the accuracy of vacancy and damage distribution profiles obtained using SRIM by comparing them with those obtained from either experimental or alternative SRIM-like codes. Owing to a lack of equipment for experimental validation, we used ion range and damage in nanostructures (iradina) code to validate SRIM results in this study. Iradina is a 3D-enabled open-source BCA code originally developed by Christian Borschel and Carsten Ronning [24] from the University of Jena as an alternative code for the simulation of ion transport. Previous studies (for example, [21], [24]) have used this code together with SRIM and confirmed that the two codes can produce results that are identical or at least close to each other. To reproduce SRIM FC results in accordance with the recommendation in the iradina manual, both the simulation and flight length types in this study were set to zero. These were done to respectively activate the iradina FC mode, and set on the standard Poisson distributed flight length and impact parameters. The ions and target parameters used in the SRIM calculations were kept the same for the corresponding iradina calculations. To make the calculations faster using the Corteo code, the scattering calculation type in iradina was set to zero, and the transport type was set to 1.

## 3 Results and Discussion

As already mentioned, an accurate estimation of the damage rates under ion irradiation is one of the key concerns in qualifying material for application in intense radiation environments such as nuclear reactors and deep space environments. In this study, we used the widely used SRIM code to predict the depth distribution profiles of primary radiation damages for He, C and O ions in FTO thin films. The results of the calculated depth-dependent vacancies for the Vac.txt and Vac.dam methods are discussed in the subsections below.

### 3.1 Vacancy Distribution Profiles: Vac.txt Versus Vac.dam Methods

Fig. 1 shows the depth-dependent calculated number of atomic vacancies (obtained from SRIM FC Vac.txt and Vac.dam methods) created within the FTO films by He, C and O ions at 10 keV, 100 keV and 1 MeV. Generally, it can be observed from Fig. 1 that for all the ions and at all ion energies, the Vac.txt method predicted higher vacancy numbers compared to Vac.dam method. Similar discrepancies between the SRIM FC Vac.txt method compared to the FC Vac.dam method have been reported by several authors (for example, [23], [29], [30], [31], [47]). The main reason for this discrepancy is associated with the differences in the methods for simulation and estimation of vacancies. In the SRIM FC Vac.txt method, sub- and near-threshold collisions are

pivotal, where replacement collision events are incorrectly classified as vacancies [23], [29], [30], [47]. This directly leads to an over-prediction of vacancy production for the SRIM FC Vac.txt method that varies by several factors depending on the bombarding particle and target mass.

Fig. 1 also shows that at each ion energy, the general depth-dependent behaviours of vacancy production for all three ions are qualitatively similar for both methods. However, the quantitative depth-dependent vacancy production behaviour for the two methods is strongly dependent on the ion energy and specific ion masses. For instance, at 10 keV kinetic energy, all three ions (He, C and O) tend to deposit most of their energies in the near-surface regions of the films. However, with the increase of ion energies, the peaks of vacancy concentrations for both methods are seen to move deeper into the material correspondingly. For He ions, the vacancy profiles for both methods have peaks at ~0.04, ~0.45 and ~2.9 μm at 10 keV, 100 keV and 1 MeV, respectively. Meanwhile, for C and O ions, the peaks are even shallower and are found at ~0.012, ~0.15 and ~1.23 μm for C ions and ~0.01, 0.12 and 1.2 μm for O ions at 10 keV, 100 keV and 1 MeV, respectively. In addition, the peak concentrations gradually shrunk with increasing ion energies and increased with the increasing atomic number from He to O at each ion energy. These suggest that elastic scattering processes are more prominent in lower energy and higher Z ions compared to higher energy and lower Z ions [29], [30].

For He ions in Fig. 1(a), the difference between the number of depth-dependent vacancies predicted by Vac.txt and Vac.dam methods at all energies appears to be small compared to those of C and O ions in Fig. 1(b) and 1(c), respectively. This particular observation was further analysed by computing and comparing the ratios of vacancies obtained from the Vac.txt method to those obtained from the Vac.dam method for He, C and O ions as shown in Fig. 2. This approach conveniently provides a way to concisely quantify the values obtained using the Vac.txt and Vac.dam methods for a wide range of ion-target conditions. It can be seen from Fig. 2 that the ratios of integrated vacancy production obtained using Vac.txt versus Vac.dam method quantitatively depict the detailed depth-dependent behaviour for all the investigated ions as shown in Fig. 1.

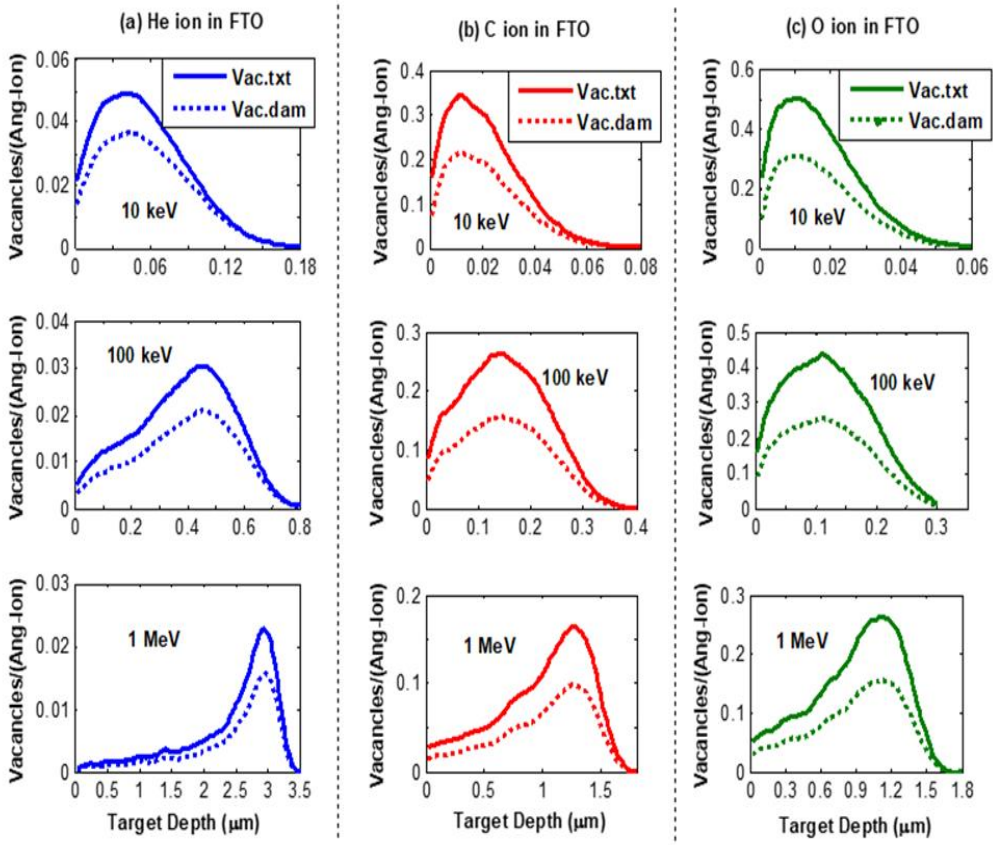


Fig. 1. Comparison between the number of vacancies obtained using SRIM FC Vac.txt and Vac.dam methods as functions of target depths for three different incident ions and ion energies.

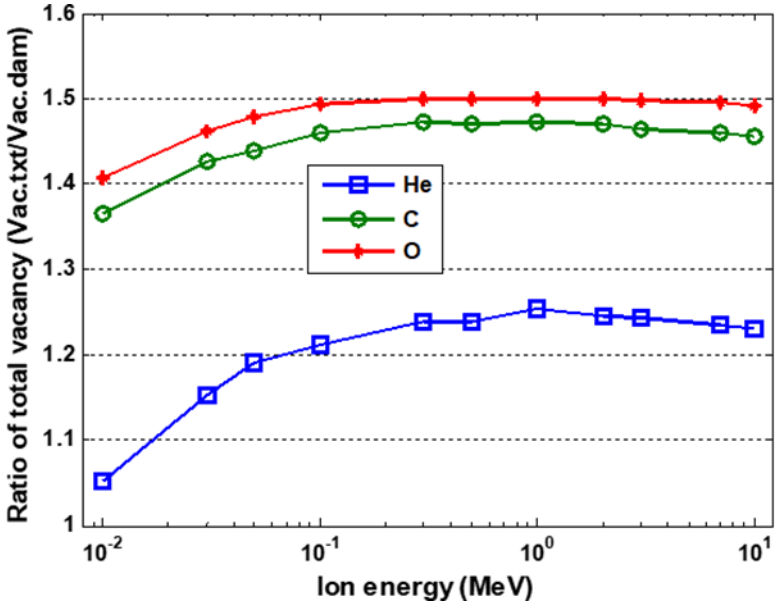


Fig. 2. The ratio of SRIM FC total vacancies obtained using the Vac.txt method to total vacancies obtained by the Vac.dam method (both integrated over the full ion range) as a function of energy for three different incident ions.

In particular, the discrepancy between the two vacancy production methods generally increased with increasing incident ion atomic number. For the case of He ions, the calculated number of vacancies for the Vac.txt and Vac.dam methods are nearly identical at all ion energies, with an average value of ~1.21. However, substantial discrepancies between the two methods are observed for C and O bombarding ions, where the Vac.txt method produced a higher number of calculated vacancies than the Vac.dam method by an average value of ~1.45 and 1.48 for C and O ions, respectively. Agarwal *et al*. [23] observed that for the SRIM FC calculation of vacancy production in compound materials, the Vac.txt prediction of vacancy production is significantly higher than the Vac.dam method by a factor of ~1.3 to 2.2, which is consistent with the findings of this study.

### 3.2 Energy Partitioning, Ion Distribution and Damage Dose Profiles

To evaluate irradiation-induced damages in FTO thin films, and the contributions of the electronic (ie energy loss due to excitation and ionisation) and nuclear-stopping powers, damage cascade simulations were performed using SRIM FC mode for all three ions and ion energies considered. For each ion type considered, the fluence to damage dose (with regard to DPA) conversions were manually done based on the damage energy approach in Equation 4. The electronic energy losses per unit of target depth for the incident He, C and O ions at three different energies as functions of depths were determined using “IONIZ.txt” SRIM FC output files by summing together ionisations

by IONS and RECOILS columns as described in [23] and [25]. On the other hand, the nuclear energy losses per unit of target depth as functions of target depths were determined using "E2RECOIL.txt" SRIM FC output files as the sum of energy absorbed by the target recoils at each depth [25]. Information about the incident ion distribution within the FTO target was obtained from the "RANGE.txt" SRIM output files. The depth-dependent energy partitioning, ion distribution, and damage dose profiles are presented in the subsections below.

### *3.2.1 Energy Partitioning and Ion Distribution Profiles*

Fig. 3, 4 and 5 show the depth-dependent electronic and nuclear energy losses, displacements per atom (damage dose), and distribution profiles of the implanted He, C and O ions respectively, as they rest in FTO thin film layers. Interestingly, it can be seen from the figures that the phenomena for the different ion types and energies are quite different. As the ions impinge on FTO thin film layers, they lose energy via electronic and nuclear collision processes as shown in Fig. 3, 4 and 5 until they come to rest. The latter process is an elastic collision process in which an incident ion loses energy through interactions with atomic nuclei, and it is the one responsible for the formation of radiation-induced damage defects in materials [42]. Conversely, electronic energy losses occur when an incident ion interacts with atomic electrons through excitation and ionisation processes [48]. Electronic energy loss can lead to the formation of localised electronic excitations, which can rupture or change the nature of covalent/ionic bonds, modify valence electron distributions, and lead to the formation of charged defects, enhanced defect and atomic mobilities, and increased system energy [48], [49]. High electronic temperatures lead to highly localised inelastic thermal spikes on the atomic lattice via electron-phonon coupling that initiates short-lived transient thermal processes, which can result in defect formation, diffusion, phase transformations, and local structures driven far from equilibrium [25]. Ion-induced damages in materials are therefore often superficially described as nuclear energy deposition (displacement cascade events) or electronic energy deposition at much higher energies.

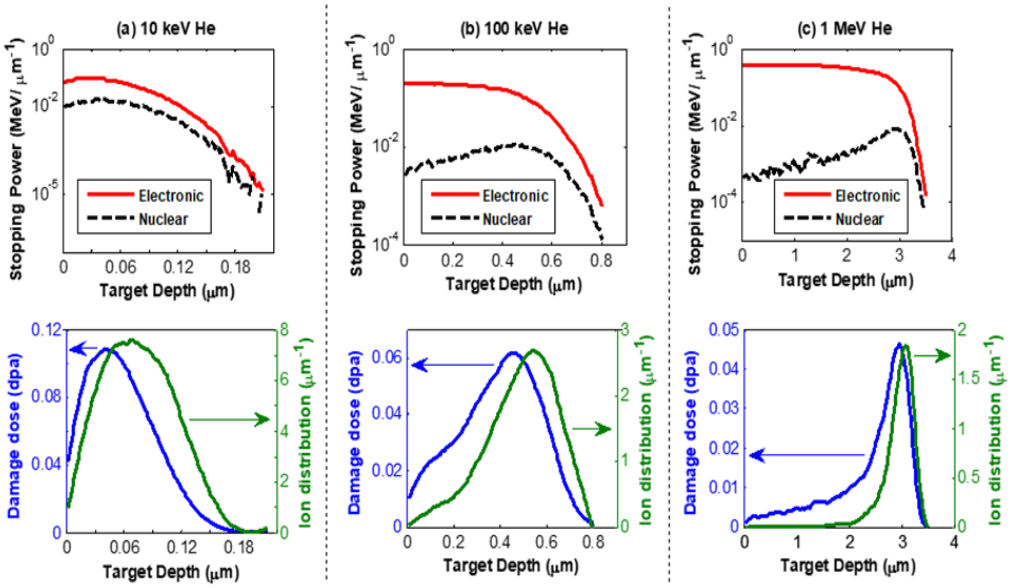


Fig. 4. Depth-dependent electronic/nuclear energy losses, damage dose and ion distribution comparisons for different He ion energies implanted in FTO film.

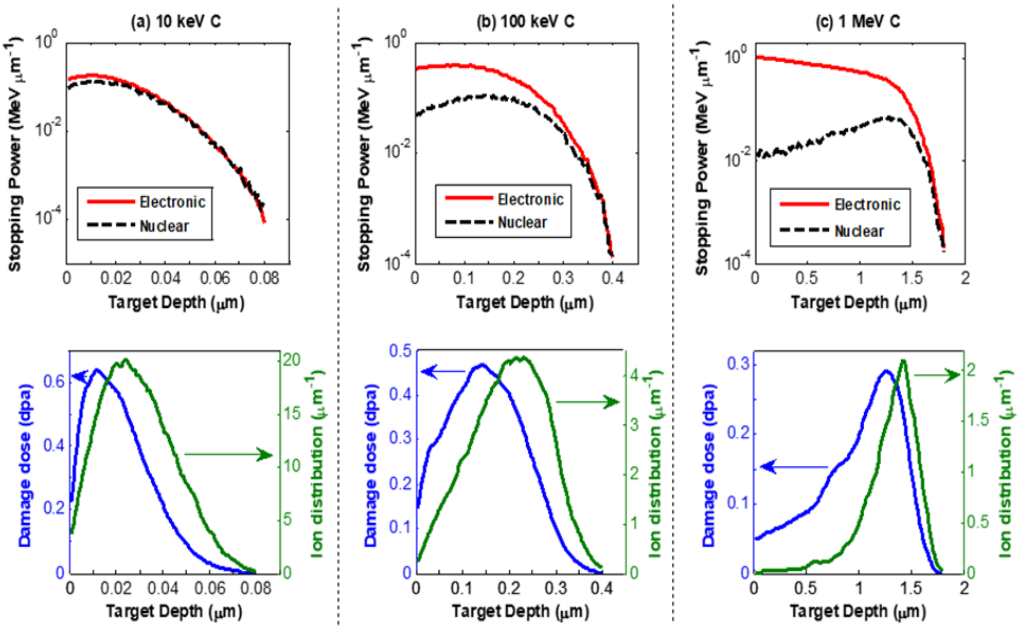


Fig. 3. Depth-dependent electronic/nuclear energy losses, damage dose and ion distribution comparisons for different C ion energies implanted in FTO film.

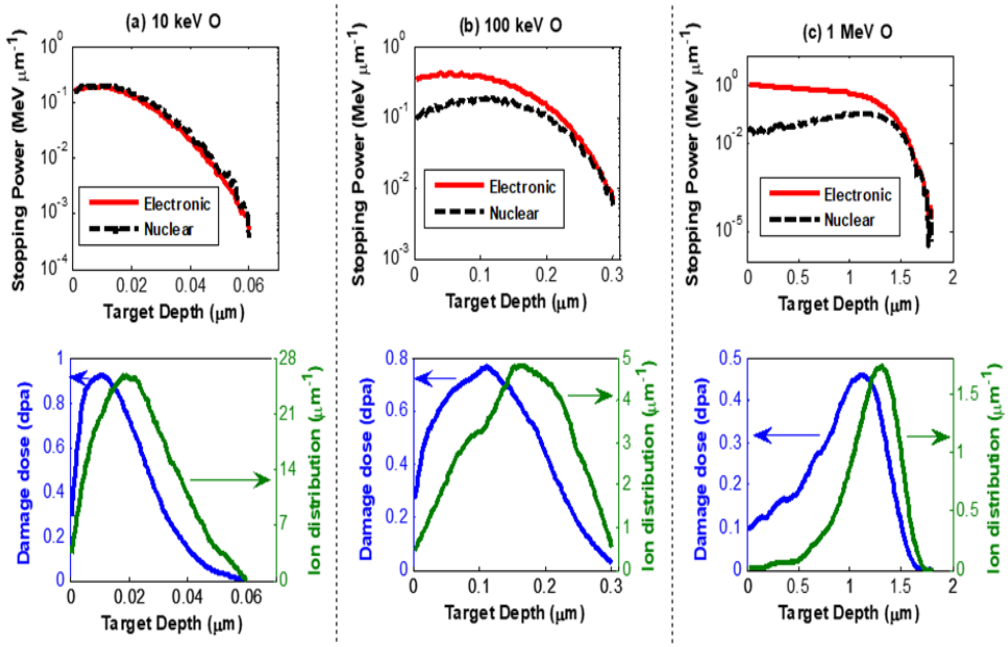


Fig. 5. Depth-dependent electronic/nuclear energy losses, damage dose and ion distribution comparisons for different O ion energies implanted in FTO film.

As can be observed from Fig. 3, 4 and 5, the contributions of electronic and nuclear energy loss mechanisms to the stopping of the incident particles depend on the type of particle and its energy. Comparing the energy partitioning features found in Fig. 3, 4 and 5, we observed the following:

- For each ion considered, its penetration depth into the FTO layers increased with increasing ion energy and decreased with increasing ion Z (at each ion energy) from He to C and O ions. To be specific, the estimated maximum ranges of 10 keV, 100 keV and 1 MeV He, C and O ions in the FTO films are approximately 0.2, 0.85 and 3.5 μm for He; 0.08, 0.4 and 1.8 μm for C; and 0.06, 0.3 and 1.8 μm for O, respectively. The observed decrease in penetration depth of the projectile ions with increasing ion atomic number is because the electronic stopping power of a higher Z projectile is larger, as the stopping power scales with Z [25], [29], [30]. This implies that large angle deflections happen more frequently with O than C and He ions because the mass of O is much larger than that of C and He. That is, O easily interacts with atomic nuclei and losses its energy more rapidly as it travels through the film layers than C and He ions.
- As the kinetic energies of the incident He, C, and O ions were increased from 10 keV, 100 keV and 1 MeV, the maximum electronic energy losses for all the ions increased, while the maximum nuclear energy losses decreased with increasing ion

energies. This implies that the principal energy loss in the middle and high energy regimes is attributed to collision with electrons.

- For all three ions and at each ion energy considered, the difference between electronic and nuclear energy losses reduces with increasing ion Z (ie the difference is greater for He than for C and O ions).
- Near the points of entry of the incident He, C and O ions into the FTO film layers (when the incoming ion energy is high), the difference between electronic and nuclear energy losses increases with increasing ion energy.
- Fig. 3, 4, 5(b) and 5(c) show that as the He, C, and O ions continue to traverse the FTO film layers and reach near the ends of their trajectories (when the ion energy is low enough), there are larger drops in electronic energy losses, and consequently the difference between nuclear and electronic energy losses become small. The energy loss due to elastic scattering first increases, and then sharply decreases and starts exhibiting a peak near the maximum penetration depth as shown at the tails of the ion trajectories, especially for the case of ions at 1 MeV kinetic energy. Nuclear stopping therefore becomes the dominant energy loss mechanism at low energy where also large angle scattering happens more frequently. In this case, the energy losses versus target depth plots begin to take the classic shape of a Bragg curve (peak) as shown in Fig. 3, 4 and 5(c). This particular observation is in good agreement with the basic nuclear stopping power theory [25].

Generally, the study of energy partitioning indicates that most of the energies of He, C and O ions were lost to electronic events (ionisation and excitations), and little to nuclear events that produce atomic displacements/vacancy defects. The study also revealed that nuclear stopping powers increase at low ion energies; one may therefore expect that most of the vacancies are produced at the end region of the ion range. In most cases, the electronic stopping powers are several times greater than the nuclear stopping powers. Consequently, most of the energy dissipation of the ion is due to electron energy transfers, which lead to cleavage of FTO crystals and local melting of materials within the hotspots around the primary ion trajectory.

However, considering separate analyses of the energy partitioning of the three ions, we observed the following:

- From Fig. 3, the electronic energy loss mechanism dominates and is much higher than the nuclear energy loss mechanism for all the three ion energies considered in this study. Also, Fig. 3(a) shows that as both the electronic and nuclear energy losses decrease with increasing ion range, the difference between the two energy loss mechanisms is comparatively uniform, with electronic energy loss being about 10 times higher than nuclear energy loss throughout the ion range.
- From Fig. 4, the electronic energy loss mechanism dominates over the nuclear energy loss mechanism, except in Fig. 4(a) (10 keV C ion) where electronic and nuclear energy losses are approximately equal near the end of the C ion range in

the film (when the C ion energy is low enough). Also, from Fig. 4(a), we observed that as both the electronic and nuclear energy losses decrease with increasing ion range, the difference between the two energy loss mechanisms is relatively small, and shrinks with increasing ion range.

- Fig. 5 shows that the electronic energy loss mechanism dominates over the nuclear energy loss mechanism, except in Fig. 5(a) (10 keV O ion) where nuclear energy loss slightly supersedes electronic energy loss throughout the ion trajectory. Also, the difference between electronic and nuclear energy losses in Fig. 4(a) is small as both decreases with increasing ion range.

### *3.2.2 Damage Dose (DPA) Profiles*

Fig. 3, 4 and 5 also show displacement damage doses (with regard to DPA) and distribution profiles of injected He, C and O ions, respectively, at three different ion energies of 10 keV, 100 keV and 1 MeV. As can be observed from the figures, damage dose profiles strongly depend on the type of incident particle and its energy. For a lighter-charged particle such as He, only isolated Frenkel pairs or small clusters are likely to be produced owing to their small mass. For heavier ions such as C and O, at the beginning of the interactions, the energy losses of the charged particles will be mainly by electronic processes. However, as the particles traverse the target, their energies will gradually decrease until a level where nuclear processes become the main cause of energy losses. For electronic dominant energy loss regimes, the particles will follow linear courses in the material with heat depositions. On the other hand, for nuclear dominant energy loss regimes, the particles will follow random courses with large deflections until they come to rest in the material. In the nuclear interaction regime, energy is dissipated mainly by the creation of large displacement cascades being the most damaging of the two processes. The spatial distribution of the damage created by heavy ions will therefore notably depend on the energy of the particles. The higher the energy, the larger the projected range in the material, the larger the range with dominant electronic energy losses, and the deeper the damage peak near the implantation zone of the ions [50].

By analysing the displacement damage dose and ion distribution profiles in Fig. 3, 4 and 5, it can generally be observed that for all three ions, the damage peaks appear at depths shallower than the peak positions of the injected ions. Also, it is observed that the longitudinal straggling ranges for ions go deeper with increasing damage dose. Table I shows the maximum estimated DPA in the projected range of 10 keV, 100 keV and 1 MeV He, C and O ions in FTO (ie in the damaged irradiated layer). From Table I, it can be seen that the maximum estimated DPA for all three ions considered decreased with increasing ion energy and increased with increasing Z at each ion energy. The observed decrease in DPA with increasing ion energy is because, at high energy, electronic energy loss is the dominant energy loss mechanism [25], [29], [30]. The observed increase in DPA with increasing ion Z is due to the greater contribution from elastic scattering by higher Z such as C and O compared to that of He [29], [30].

As mentioned earlier, DPA is typically the statistical average of the fractional number of lattice atoms that have been displaced. According to Huguet-Garcia [50], the mean value of damage dose that can cause amorphisation of irradiated material (dose to amorphisation or simply DTA) is ~0.4 DPA. As can be seen from Table I, the estimated doses for 10 and 100 keV O ions are higher than the dose for the amorphisation value. Consequently, one would imagine that at these energies O ions could have caused the amorphisation of the FTO film crystals. Based on the DPA values in Table I, it can be suggested that significant fractions of atoms in the irradiated FTO layers experienced lattice displacements, with 10 and 100 keV O ions resulting in amorphisation.

TABLE I
MAXIMUM ESTIMATED DPA IN THE PROJECTED RANGE OF 10 000 INCIDENT He, C AND O IONS AT DIFFERENT ENERGIES

| **Ion energy [keV]** | **DPA** | | |
|---|---|---|---|
| | **He** | **C** | **O** |
| 10 | 0.06 | 0.38 | 0.55 |
| 100 | 0.04 | 0.26 | 0.43 |
| 1 000 | 0.03 | 0.16 | 0.27 |

### 3.3 Comparison Between SRIM and Iradina Vacancies

To validate the SRIM results obtained in this study, depth profiles of vacancies and implanted ions with different ion energies obtained from SRIM simulation outputs were compared with those obtained from iradina calculations. Both codes were operated in the FC mode, and the number of vacancies used in the comparisons was obtained using the damage energy approach. Information about the iradina calculated total incident ion distribution within the target was obtained from “ira.ions.total” iradina output text files. The iradina calculated total damage energy was obtained from “ira.energy.phonons” iradina output text files. Since iradina computation is similar to that of SRIM, the results of these two codes are expected to be comparable, and this can serve as a basic test to verify the correct functionality of one SRIM code. Fig. 6 shows the depth distributions of implanted He, C and O ions as predicted by SRIM and iradina codes, while Fig. 7 shows the SRIM and iradina depth profiles of the number of vacancies created by He, C and O ion irradiations of FTO thin film at different ion energies.

Generally, we observed that for all the three ions and ion energies considered in this study, the peaks of implanted ion concentration (Fig. 6) and vacancy concentration (Fig. 7) move deeper correspondingly as the kinetic energies of the implanted ions are increased. In addition, their peak concentrations gradually shrink with increasing ion energy. Also, nearly perfect agreements between SRIM and iradina are found in the predictions of depth distributions of implanted ions as shown in Fig. 6. Only slight deviations are observed in the O ion projected ranges (depths of peak concentrations) predicted by SRIM and iradina. However, for the case of vacancy distribution profiles

shown in Fig. 7, somewhat good, though not perfect agreements are observed between SRIM and iradina, with SRIM yielding a slightly higher number of vacancies than iradina calculations for all three ions and ion energies considered. Similar observations of good agreement between SRIM and iradina have been observed by [21], [24], and [35]. The slight discrepancies observed between SRIM and iradina calculated vacancies can be attributed to the approaches the two codes used to calculate scattering angles and stopping powers [24], [35]. Iradina uses the open-source Corteo code to calculate scattering angles and stopping powers from precalculated tables with a fast-indexing mechanism, whereas SRIM uses the MAGIC algorithm [24].

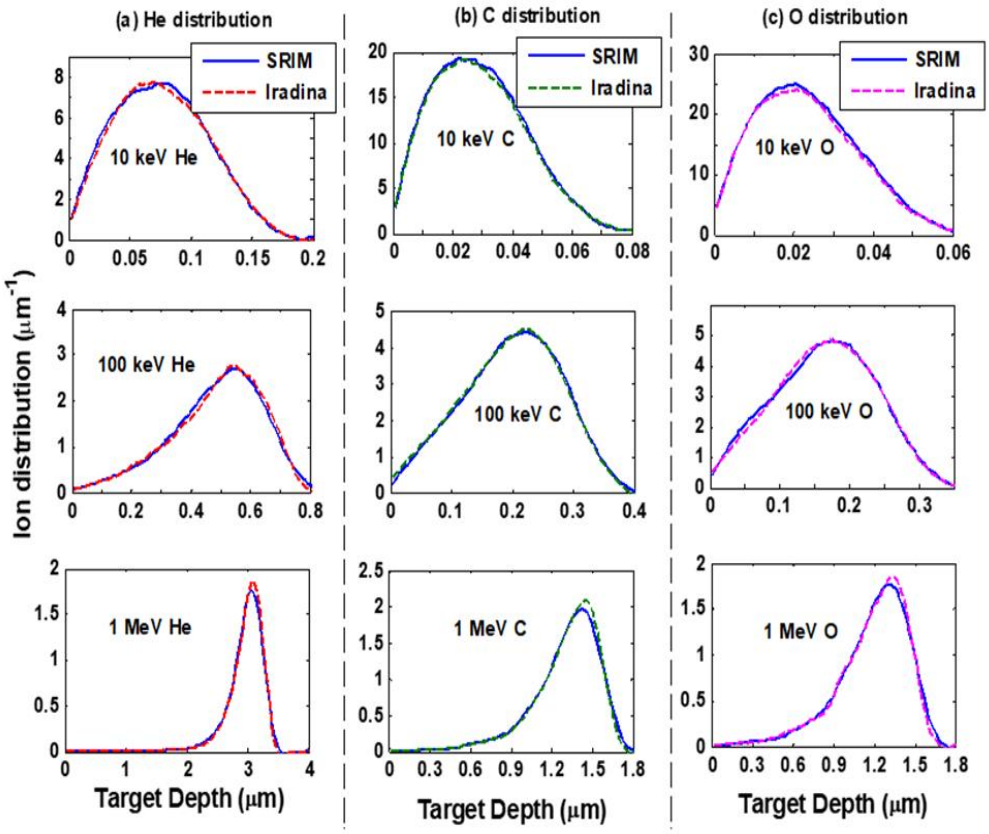


Fig. 6. Comparison of SRIM and iradina simulated depth distribution profiles of He, C and O ions.

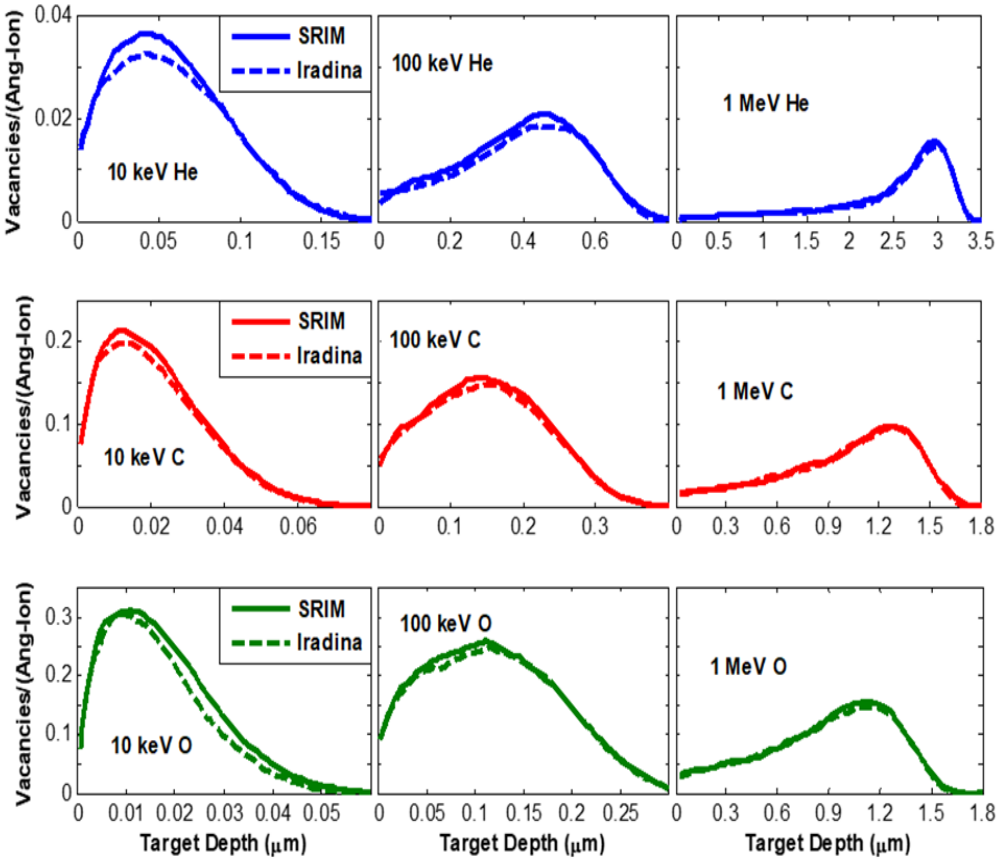


Fig. 7. Comparison of SRIM and iradina calculated depth-dependent vacancies created by He, C and O ions.

## 4 Conclusion

SRIM simulations of vacancy distribution, energy partitioning, damage dose and distribution profiles of the implanted He, C and O ions into the FTO films were performed at three different ion energies of 10 keV, 100 keV and 1 MeV using SRIM-2013 operated in the FC mode. From these simulations, it was generally found that the depth penetration power of the incident ions increased with increasing ion energy and decreased with increasing ion mass. Meanwhile, the peak concentrations shrink with increasing ion energies and increase with the increasing atomic numbers from He to C and O at each ion energy. By comparing the number of vacancies directly calculated from the "VACANCY.TXT" files (Vac.txt method) and those calculated using the damage energy approach (Vac.dam method), it was found that for all the ions and at all ion energies considered in this study, Vac.txt method over predicted the vacancies

compared to Vac.dam method. The discrepancies between the number of vacancies obtained from Vac.txt and Vac.dam methods were generally found to increase with increasing incident ion atomic number.

Analysis of energy partitioning profiles indicated that most of the energies of He, C and O ions were lost to electronic events (ionisation and excitations), and little to nuclear events that produce atomic displacements/vacancy defects. The study also revealed that nuclear stopping powers increase at low ion energies. Consequently, one may expect that most of the vacancies are produced at the end region of the ion range. In most cases, the electronic stopping powers are several times greater than the nuclear stopping powers. In this study, we also found that damage dose profiles strongly depend on the type of incident particle and its energy and that significant fractions of atoms in the irradiated FTO layers experienced lattice displacements. A comparison of SRIM and iradina calculated vacancies and incident ion distribution profiles generally showed perfect agreements between SRIM and iradina for such calculations.

## 5 References

[1] Z. Y. Banyamin, P. J. Kelly, G. West and J. Boardman, "Electrical and optical properties of fluorine doped tin oxide thin films prepared by magnetron sputtering," *Coatings*, vol. 4, no. 4, pp. 732–746, 2014, doi: 10.3390/coatings4040732.

[2] F. I. Chowdhury, T. Blaine and A. B. Gougam, "Optical transmission enhancement of fluorine doped tin oxide (FTO) on glass for thin film photovoltaic applications," *Energy Procedia*, vol. 42, pp. 660–669, 2013, doi: 10.1016/j.egypro.2013.11.068.

[3] K. Zeng, F. Zhu, J. Hu, L. Shen, K. Zhang and H. Gong, "Investigation of mechanical properties of transparent conducting oxide thin films," *Thin Solid Films*, vol. 443, nos 1–2, pp. 60–65, 2003, doi: 10.1016/S0040-6090(03)00915-5.

[4] L. T. C. Tuyen, S. R. Jian, N. T. Tien and P. H. Le, "Nanomechanical and material properties of fluorine-doped tin oxide thin films prepared by ultrasonic spray pyrolysis: Effects of F-doping," *Materials*, vol. 12, no. 10, 2019, doi: 10.3390/ma12101665.

[5] A. Adjimi, M. L. Zeggar, N. Attaf and M. S. Aida, "Fluorine-doped tin oxide thin films deposition by sol-gel technique, *JCPT*, vol. 8, no. 4, pp. 89–106, 2018, doi: 10.4236/jcpt.2018.84006.

[6] M. Batzill and U. Diebold, "The surface and materials science of tin oxide," *Prog. Surf. Sci.*, vol. 79, nos 2–4, pp. 47–154, 2005, doi: 10.1016/j.progsurf.2005.09.002.

[7] N. Lavanya *et al.*, "Investigations on the effect of gamma-ray irradiation on the gas sensing properties of $SnO_2$ nanoparticles," *Nanotechnol.*, vol. 27, no. 38, pp. 1–9, 2016, doi: 10.1088/0957-4484/27/38/385502.

[8] A. Sharma, M. Varshney, K. D. Verma, Y. Kumar and R. Kumar, "Structural and surface microstructure evolutions in SnO thin films under ion irradiation," *NIM-B*, vol. 308, pp. 15–20, 2013, doi: 10.1016/j.nimb.2013.04.054.

[9] M. M. Mikhailov, A. N. Lapin, S. A. Yuryev and V. V. Karanskiy, "Effect of proton irradiation on the optical properties of coating based on ZnO powder and liquid $K_2SiO_3$," *Surf. Coat. Technol.*, vol. 387, p. 125548, 2020, doi: 10.1016/j.surfcoat.2020.125548.

[10] J. N. Pelton and F. Allahdadi, "Introduction," in *Handbook of Cosmic Hazards and Planetary Defense*, Cham: Springer, 2015, pp. 3–33, doi: 10.1007/978-3-319-03952-7.

[11] A. Takahashi, H. Ikeda and Y. Yoshida, "Role of high-linear energy transfer radiobiology in space radiation exposure risks," *Int. J. Part. Ther.*, vol. 5, no. 1, pp. 151–159, 2018, doi: 10.14338/IJPT-18-00013.1.

[12] I. G. Madiba, N. Émond, M. Chaker, F. T. Thema, S. I. Tadadjeu and U. Muller, "Effects of gamma irradiations on reactive pulsed laser deposited vanadium dioxide thin films," *Appl. Surf. Sci.*, vol. 411, pp. 271–278, 2017, doi: 10.1016/j.apsusc.2017.03.131.

[13] B. Oryema *et al.*, "Effects of 7 MeV proton irradiation on microstructural, morphological, optical, and electrical properties of fluorine-doped tin oxide thin films," *Surf. Interfaces*, vol. 28, 2022, doi: 10.1016/j.surfin.2021.101693.

[14] S. K. Sen *et al.*, "An investigation of $^{60}$Co gamma radiation-induced effects on the properties of nanostructured α-$MoO_3$ for the application in optoelectronic and photonic devices," *Opt. Quantum Electron.*, vol. 51, no. 82, pp. 1–15, 2019, doi: 10.1007/s11082-019-1797-9.

[15] Y. G. Li, Y. Yang, M. P. Short, Z. J. Ding, Z. Zeng and J. Li, "IM3D: A parallel Monte Carlo code for efficient simulations of primary radiation displacements and damage in 3D geometry," *Sci. Rep.*, vol. 5, pp. 1–13, 2015, doi: 10.1038/srep18130.

[16] B. Yang *et al.*, "PKA distributions in InAlAs and InGaAs materials irradiated by protons with different energies," *NIM-B*, vol. 484, pp. 42–47, 2020, doi: 10.1016/j.nimb.2020.09.024.

[17] C. J. Ortiz, "A combined BCA-MD method with adaptive volume to simulate high-energy atomic-collision cascades in solids under irradiation," *Comput. Mater. Sci.*, vol. 154, pp. 325–334, 2018, doi: 10.1016/j.commatsci.2018.07.058.

[18] I. Santos, L. A. Marqús, L. Pelaz and P. López, "Improved atomistic damage generation model for binary collision simulations," *J. Appl. Phys.*, vol. 105, no. 8, pp. 1–8, 2009, doi: 10.1063/1.3110077.

[19] G. S. Was, "Challenges to the use of ion irradiation for emulating reactor irradiation," *J. Mater. Res.*, vol. 30, no. 9, pp. 1158–1182, 2015, doi: 10.1557/jmr.2015.73.

[20] K. Nordlund, “Historical review of computer simulation of radiation effects in materials,” *J. Nucl. Mater.*, vol. 520, pp. 273–295, 2019, doi: 10.1016/j.jnucmat.2019.04.028.

[21] J. Crocombette and C. van Wambeke, “Quick calculation of damage for ion irradiation: Implementation in Iradina and comparisons to SRIM,” *EPJ Nuclear Sci. Technol.*, vol. 5, no. 7, 2019, doi: 10.1051/epjn/2019003.

[22] W. Eckstein, “The binary collision model,” in *Computer Simulation of Ion-Solid Interactions*. Berlin: Springer, pp. 4–32, 1991, doi: 10.1007/978-3-642-73513-4_2.

[23] S. Agarwal, Y. Lin, C. Li, R. E. Stoller and S.J. Zinkle, “On the use of SRIM for calculating vacancy production: Quick calculation and full-cascade options,” *NIM-B*, vol. 503, pp. 11–29, 2021, doi: 10.1016/j.nimb.2021.06.018.

[24] C. Borschel and C. Ronning, “Ion beam irradiation of nanostructures—A 3D Monte Carlo simulation code,” *NIM-B*, vol. 269, no. 19, pp. 2133−2138, 2011, doi: 10.1016/j.nimb.2011.07.004.

[25] Y. Zhang and W. J. Weber, “Ion irradiation and modification: The role of coupled electronic and nuclear energy dissipation and subsequent nonequilibrium processes in materials,” *Appl. Phys. Rev.*, vol. 7, no. 4, pp. 1–35, 2020, doi: 10.1063/5.0027462.

[26] Y.G. Li, Q. R. Zheng, L. M. Wei, C. G. Zhang and Z. Zeng, “A review of surface damage/microstructures and their effects on hydrogen/helium retention in tungsten,” *Tungsten*, vol. 2, no. 1, pp. 34–71, 2020, doi: 10.1007/s42864-020-00042-w.

[27] K. Nordlund *et al*., “Primary radiation damage in materials review of current understanding and proposed new standard displacement damage model to incorporate in cascade defect production efficiency and mixing effects,” NEA/NSC/DOC, 9, Nuclear Energy Agency of the OECD, 2015.

[28] M. Guthoff, W. de Boer and S. Müller, “Simulation of beam induced lattice defects of diamond detectors using FLUKA,” *NIM-A*, vol. 735, pp. 223–228, 2014, doi: 10.1016/j.nima.2013.08.083.

[29] U. Saha, K. Devan, A. Bachchan, G. Pandikumar and S. Ganesan, “Neutron radiation damage studies in the structural materials of a 500 MWe fast breeder reactor using DPA cross-sections from ENDF/B-VII.1,” *Pramana J. Phys.*, vol. 90, no. 4, pp. 1–15, 2018, doi: 10.1007/s12043-018-1536-y.

[30] U. Saha, K. Devan and S. Ganesan, “A study to compute integrated dpa for neutron and ion irradiation environments using SRIM-2013,” *J. Nucl. Mater.*, vol. 503, pp. 30–41, 2018, doi: 10.1016/j.jnucmat.2018.02.039.

[31] R. E. Stoller, M. B. Toloczko, G. S. Was, A. G. Certain, S. Dwaraknath and F. A. Garner, “On the use of SRIM for computing radiation damage exposure,” *NIM-B*, vol. 310, pp. 75–80, 2013, doi: 10.1016/j.nimb.2013.05.008.

[32] M. A. Amirkhani and F. Khoshahval, “Evaluation of the radiation damage effect on mechanical properties in Tehran research reactor (TRR) clad,” *Nucl. Eng. Technol.*, vol. 52, no. 12, pp. 2975–2981, 2020, doi: 10.1016/j.net.2020.05.028.

[33] G. H. Kinchin, “The displacement of atoms in solids during irradiation,” *Solid State Phys.*, vol. 2, p. 307, 1956.

[34] M. J. Norgett, M. T. Robinson and I. M. Torrens, “A proposed method of calculating displacement dose rates,” *Nucl. Eng. Des.*, vol. 33, no. 1, pp. 50–54, 1975, doi: 10.1016/0029-5493(75)90035-7.

[35] S. Chen and D. Bernard, “On the calculation of atomic displacements using damage energy,” *Results Phys.*, vol. 16, p. 102835, 2020, doi: 10.1016/j.rinp.2019.102835.

[36] J. P. Crocombette, L. van Brutzel, D. Simeone and L. Luneville, “Molecular dynamics simulations of high energy cascade in ordered alloys: Defect production and subcascade division,” *J. Nucl. Mater.*, vol. 474, pp. 134–142, 2016, doi: 10.1016/j.jnucmat.2016.03.020.

[37] K. Nordlund *et al.*, “Improving atomic displacement and replacement calculations with physically realistic damage models,” *Nat. Commun.*, vol. 9, no. 1, pp. 1–8, 2018, doi: 10.1038/s41467-018-03415-5.

[38] J. F. Ziegler, M. D. Ziegler and J. P. Biersack, “SRIM—The stopping and range of ions in matter (2010),” *NIM-B*, vol. 268, nos 11–12, pp. 1818–1823, 2010, doi: 10.1016/j.nimb.2010.02.091.

[39] J. C. Chancellor *et al.*, “Limitations in predicting the space radiation health risk for exploration astronauts,” *NPJ Microgravity*, vol. 4, no. 1, pp. 1–11, 2018, doi: 10.1038/s41526-018-0043-2.

[40] M. Maalouf, M. Durante and N. Foray, “Biological effects of space radiation on human cells: History, advances and outcomes,” *Journal of Radiation Research*, vol. 52, no. 2, pp. 126–146, 2011, doi: 10.1269/jrr.10128.

[41] W. Z. Samad, M. M. Salleh, A. Shafiee and M. A. Yarmo, “Structural, optical and electrical properties of fluorine doped tin oxide thin films deposited using inkjet printing technique,” *Sains Malaysiana*, vol. 40, no. 3, pp. 251–257, 2011.

[42] M. J. Madito, T. T. Hlatshwayo, V. A. Skuratov, C. B. Mtshali, N. Manyala and Z. M. Khumalo, “Characterization of 167 MeV Xe ion irradiated n-type 4H-SiC,” *Appl. Surf. Sci. J.*, 2019, doi: 10.1016/j.apsusc.2019.07.147.

[43] Y. Kudriavtsev, A. Villegas, A. Godines and R. Asomoza, “Calculation of the surface binding energy for ion sputtered particles,” *Appl. Surf. Sci.*, vol. 239, nos 3–4, pp. 273–278, 2005, doi: 10.1016/j.apsusc.2004.06.014.

[44] A. Y. Konobeyev, U. Fischer, Y. A. Korovin and S. P. Simakov, “Evaluation of effective threshold displacement energies and other data required for the calculation of advanced atomic displacement cross-sections,” *Nucl. Energy Technol.*, vol. 3, no. 3, pp. 169–175, 2017, doi: 10.1016/j.nucet.2017.08.007.

[45] Y. Zhang *et al*., “Response of strontium titanate to ion and electron irradiation,” *J. Nucl. Mater.*, vol. 389, no. 2, pp. 303–310, 2009, doi: 10.1016/j.jnucmat.2009.02.014.

[46] K. G. McCracken, G. A. Dreschhoff, E. J. Zeller, D.F. Smart and M. A. Shea, “Solar cosmic ray events for the period 1561–1994: Identification in polar ice, 1561–1950,” *J. Geophys. Res.*, vol. 106, no. A10, pp. 21585–21598, 2001, doi: 10.1029/2000JA000237.

[47] M. I. Bratchenko, V. V. Bryk, S. V. Dyuldya, A. S. Kalchenko, N. P. Lazarev and V. N. Voyevodin, “Comments on DPA calculation methods for ion beam driven simulation irradiations,” *Probl. Atom. Sci. Technol.*, vol. 2, pp. 11–16, 2013.

[48] G. S. Was and P. L. Andresen, “Radiation damage to structural alloys in nuclear power plants: Mechanisms and remediation,” *Structural Alloys for Power Plants: Operational Challenges and High-Temperature Materials*, pp. 355–420, 2014, doi: 10.1533/9780857097552.2.355.

[49] M. Nastasi and J. W. Mayer, *Ion Implantation and Synthesis of Materials*. Springer, 2006.

[50] J. Huguet-Garcia, “In situ and ex situ characterization of the ion-irradiation effects in third generation SiC fibers,” PhD thesis, Dept Phys. Chem. Mater., UPMC, Paris, 2015 https://theses.hal.science/tel-01230902v1/file/2015PA066221.pdf.